Macromolecules **2004,** *37,* 7265−7277

Probing the Melting Behavior of a Homogeneous Ethylene/1-Hexene Copolymer by Small-Angle Light Scattering

Ying Li and Yvonne A. Akpalu*

Department of Chemistry & Chemical Biology, Rensselaer Polytechnic Institute, Troy, New York 12180

Received March 23, 2004; Revised Manuscript Received June 9, 2004

ABSTRACT: The melting behavior of a homogeneous ethylene/1-hexene copolymer ($M_w = 70\,000$ g/mol; $\rho = 0.90$ g/cm^3; 6.4 mol % hexene) is studied by the simultaneous measurement of small-angle light scattering (SALS) under cross-polarized (H_V) or parallel-polarized (V_V) optical alignments and transmitted light. The temperature variation of H_V and V_V patterns and integrated intensities during melting is consistent with the predictions of a generalized SALS model presented. The data show that H_V and V_V SALS can be used to determine the number of crystal populations, the melting temperature of each crystal population, and the spatial organization of crystalline aggregates. For a given crystallization condition, the final melting temperature ($T_m{}^f = 114$ °C) obtained from H_V and V_V SALS is in good agreement with values obtained from differential scanning calorimetry and small-angle X-ray scattering (SAXS) measurements on thicker samples with the same thermal history. The thickness of the largest crystals that can form ($l_f = 11$ nm) is determined from Guinier plots of the SAXS profiles obtained during the final stage of melting. The equilibrium melting temperature ($T_m{}^c = 136 \pm 2$ °C) calculated from the modified Gibbs−Thomson relation with the $T_m{}^f$ and l_f values obtained is consistent with the value ($T_m{}^c = 134$ °C) predicted from the Flory's equilibrium theory of melting for a random copolymer with 6.4 mol % comonomer. Our results demonstrate that SALS can be used to understand and provide a quantitative description of how crystallization conditions affect the supermolecular structure organization in copolymers of ethylene and α-olefins.

Introduction

In recent years, substantial progress has been made in understanding the crystallization and melting behavior of copolymers of ethylene and α-olefins (EOCs). In particular, random homogeneous ethylene/α-olefin copolymers (*ran*-EOCs) have made it possible to study[1−5] the crystallization and melting behavior systematically as a function of the comonomer composition by avoiding the ill-defined chain microstructure of heterogeneous copolymers obtained with conventional Ziegler−Natta catalysts.[6−17] Differential scanning calorimetry (DSC) has been widely used in such studies[2,3,18−24] to monitor the melting of EOCs as a function of crystallization conditions. Multiple melting behavior has been observed but the origin of the endothermic peaks and the spatial (micrometer scale and nanoscale) organization of crystals cannot be determined solely from the measurements. Usually, separate microscopic (optical, scanning electron, transmission electron, and atomic force microscopy) measurements[3,24,25] are usually performed on room-temperature specimens to observe the prominent morphological features present in the samples. These micrographs, however, do not provide enough information to correlate all the melting characteristics of the morphological units.

Scattering measurements provide a means to quantify the fractions and sizes of morphological units.[26−30] Extensive small-angle X-ray scattering (SAXS) studies have been conducted to follow structural changes during crystallization and melting of EOCs.[4,5,30−32] These studies have demonstrated the importance of SAXS for understanding thermodynamic and kinetic factors affecting the development the lamellar (nanoscale) morphology of semicrystalline polymers. Scattering data at very small angles, possible with ultra small-angle X-ray scattering[33] or small-angle light scattering (SALS),[30] is necessary to investigate the spatial arrangement of micrometer crystalline aggregates or superstructures. Some recent studies[30,34−36] have demonstrated that time-resolved, polarization dependent SALS is very sensitive to micrometer scale density and orientation fluctuations arising during polymer crystallization. There are relatively few reported SALS melting studies[4,37,38] for semicrystalline polymers although the variation of the refractive index contrast during melting of micrometer aggregates of high and lower melting crystals usually formed for EOCs is well suited for SALS measurements.

For EOCs, the presence of short chain branches (SCBs, e.g., methyl, ethyl, hexyl) suppresses crystal growth in one or more lateral dimensions and reduce the melting temperature and crystallinity.[1,3,6,19,23−25,39,40] The extent of this suppression increases with increasing comonomer content (decreasing density) since the number of ethylene sequences long enough to form chain-folded lamellae decreases. Thus, the lamellar morphological units and the corresponding supermolecular structures formed for an EOC depend on the branch content. Several extensive studies[23−25,30,39,41] indicate that copolymers with low comonomer content or high densities ($\rho > 0.93$ g/cm^3) form well-developed lamellae which organize to form spherulites as observed for high-density polyethylene. At higher comonomer contents or lower densities ($\rho < 0.93$ g/cm^3), small spherulites or coexisting lamellae and granular base morphologies are observed. For very low-density EOCs ($\rho \ll 0.89$ g/cm^3), it has been inferred that crystals may be organized as fringed-micelles ("bundlelike" crystalline aggregates)[25,42] or as clusters of loosely packed ethylene units.[41] In addition, a diverse range of superstructures can be

---

* To whom correspondence should be addressed. E-mail: akpaly@rpi.edu.

10.1021/ma049435n CCC: $27.50

obtained for a given copolymer by varying the crystallization conditions.[27,43,44] Multiple coexisting superstructures are obtained for EOCs because at a given crystallization temperature, ethylene sequences that are unable to crystallize are excluded from the growing crystal. These shorter sequences may either aggregate into micrometer scale domains surrounding the crystalline regions within the superstructure formed or reside between superstructures. As the crystallization temperature is lowered, these sequences crystallize to form smaller crystals. Regions rich in the aggregates of smaller crystals formed from these sequences may be large enough to be classified as separate superstructures. Thus, a technique that can characterize the complex supermolecular structures of EOCs as a function of crystallization conditions is necessary.

Morphological parameters that describe the volume fraction of superstructures (x_S) and the crystalline fraction within superstructures (x_{CS}) can be monitored by SALS during crystallization and melting.[5,26−30] If all crystals are within superstructures, the mass fraction crystallinity (w_c) from wide-angle X-ray scattering (WAXS) or DSC is proportional to the product $x_S x_{CS}$. Since SALS provides a statistical evaluation of the shapes and sizes of scattering entities (spherulites and other superstructures), poorly defined superstructures[15,25−27,44] typical for EOCs can be studied. SALS under cross-polarized optical alignment (H_V) measures orientation fluctuations arising from the arrangement of crystalline aggregates, while SALS under parallel-polarized optical alignment (V_V) measures both density and orientation fluctuations. Fluctuations in refractive index (density) arise from spatial variation in the crystalline volume fraction. The H_V and V_V invariants (total integrated intensities) can also be written in terms of x_S and x_{CS}.[28,30,38,45] This property makes the SALS invariants powerful tools for monitoring how structure develops during crystallization and melting.

In this paper, we show that SALS measurements during melting of a homogeneous ethylene/1-hexene copolymer ($M_w = 70\,000$ g/mol; $\rho = 0.90$ g/cm^3; 6.4 mol % hexene) can be used to determine the number of crystal populations, the melting temperature of each crystal population, and the spatial organization of crystalline aggregates. The final melting temperature (T_m^f) of crystalline aggregates can also be measured by SALS.

Experimental Section

The ethylene/1-hexene copolymer (EH064) studied was provided by ExxonMobil. EH064 was prepared with a metallocene catalyst. The weight-average molar mass (M_w) of EH064 is 70 000 g/mol. The polydispersity is 2.0 and the density is 0.90 g/cm^3. The mole percent of 1-hexene in the copolymer is 6.4%. Before any further sample preparation, 3 g of EH064 was dissolved in 300 mL of refluxing toluene at 110 °C. The solution was poured into an acetone/methanol (50/50) mixture (800 mL) at 0 °C. The resulting precipitate was filtered, washed, and dried under vacuum at 40−50 °C for 72 h. Additives in EH064 were removed during this procedure.

EH064 films were prepared by solvent casting from *p*-xylene (Fisher Scientific, certified). Polymer solutions at constant mass concentration of 2% (for SALS and DSC measurements) and 0.5% (for polarized optical microscopy (POM) measurements) were cast in Teflon dishes. The solutions were air-dried overnight and further dried in a vacuum oven at 50 °C and 760 Torr for 3 days to remove residual solvent. For X-ray measurements, films (~1 mm thick) were prepared by melting samples in a vacuum oven at 160 °C for 5 min. Melted samples were removed from the oven and air-cooled to room temperature.

Before any measurements, samples for SALS, DSC, POM, and X-ray scattering were first melted at 160 °C for 10 min under nitrogen to remove any thermal history, and then rapidly cooled (at 50 °C/min) to a crystallization temperature (T_c). After isothermal crystallization at T_c for 0 to 72 h, samples were rapidly cooled (at ~80 °C/min) to room temperature. This procedure was performed for T_c's ranging from 81 to 110 °C. The cooling rates were chosen to be as fast as possible with minimal temperature overshooting (<1 °C). By employment of such procedures, aggregates of crystals formed during isothermal crystallization could be distinguished from crystals that formed when samples were rapidly cooled after crystallization.[2] All the melting and cooling procedures were performed on a computer interfaced Instec HCS600V hot stage to minimize sample movement and temperature fluctuations.

DSC measurements were performed on 1.8 ± 0.1 mg (two to four stacks of films) samples sealed in aluminum pans. There were no observable effects of film stacking on DSC thermograms when samples were melted at 160 °C for 10 min before crystallization. After crystallizing samples at T_c and cooling to room temperature, the samples were stored at room temperature for less than 12 h. Melting measurements were then performed on a Mettler-Toledo DSC 822e by heating samples from −30 to +160 °C at 10 °C/min under a nitrogen atmosphere. Temperature and enthalpy values were calibrated using indium as a standard.

SALS and POM measurements were performed on film samples sealed between two round glass coverslips. An optical microscope (Olympus BX51) coupled to an Insight digital camera was used to characterize the solid-state morphology of film samples (~15 μm thick) before melting. For both SALS and X-ray scattering measurements, an Instec HCS600V hot stage was used to control the temperature to within 0.1 °C. SALS patterns under cross-polarized (H_V) and parallel-polarized (V_V) optical alignments and transmitted light were recorded using a vertical light scattering apparatus described previously.[38] The usable span of scattering vector magnitudes ($q = 4\pi(\sin\theta)/\lambda$ and 2θ is the scattering angle) was in the range 0.05 μm^{-1} < q < 2.4 μm^{-1}. Samples were heated from 30 to 160 °C under nitrogen. To optimize the data collection for scattering measurements, a heating rate of 2.5 °C/min was used. The scattering observed from SALS did not depend on heating rate within the range of 2.5 to 10 °C/min. SALS data were collected in 3−10 s time blocks.

The percent transmission was determined from the ratio of the transmitted light intensity measured with a sample in the beam path to that measured without the sample. Experimental scattering intensities from SALS were corrected for sample-to-detector distance and incident intensity variations. Corrections for reflection, refraction, and illuminated volume were also applied to the experimental intensities using methods described previously.[46] The melt contribution to the integrated intensity from H_V and V_V measurements was subtracted after accounting for statistical fluctuations. The integrated intensity calculated represents fluctuations during melting and will be referred to as a relative invariant.

SAXS and WAXS measurements were performed at a wavelength of 1.602 Å at the X10A beamline at Brookhaven National Laboratory. Film samples (~1 mm thick) wrapped in aluminum foil were heated from 30 to 160 °C at 2.5 °C/min. The scattering observed from SAXS and WAXS does not depend on heating rate within the range of 1 to 2.5 °C/min. A Bruker Hi-Star two-dimensional CCD camera (10 cm × 10 cm, 1024 × 1024 pixels) was used to collect the data. A helium chamber was placed between the sample and the detector to reduce air scattering and absorption. The usable span of scattering vector magnitudes ($q = 4\pi(\sin\theta)/\lambda$ and 2θ is the scattering angle) for WAXS was 0.22 Å^{-1} < q < 2.9 Å^{-1} and that for SAXS was 0.012 Å^{-1} < q < 0.17 Å^{-1}. NIST standards SRM 676 (α-Al_2O_3), SRM 660 (Lanthanum hexaboride), and Lupolen standard were used for angular calibration of the WAXS detector.[47] A parallel plate-ionizing detector placed before the sample cell was used to record the incident intensity.

The experimental intensities were corrected for background scattering from the camera, empty cell, incident intensity variations, and pixel-by-pixel detector sensitivity. The latter was established from the scattering of an Fe source. Data were collected in 60 and 15 s time blocks for SAXS and WAXS, respectively.

Lamellar morphological variables can be obtained from the analysis of SAXS data by an intensity model[48−50] or in real space using correlation functions.[51,52] Detailed descriptions of the correlation function[47] and intensity model[48] methods used to analyze the SAXS data obtained have been given previously. The long period (L), average crystal (l_c) and amorphous (l_a) thicknesses obtained from both methods were the same within 0.01 nm.

SALS Model

Spherulites are usually formed when polymers crystallize from the melt. Experimental H_V and V_V SALS patterns for spherulites can be predicted by calculating scattering patterns for objects with definite shape such as anisotropic spheres or disks.[53−58] For many semicrystalline polymers, experimental scattering patterns deviate substantially from that of model predictions because of several morphological features (e.g., incomplete spherulites and high internal disorder) of ill-defined spherulites.[25,39,44] During crystallization and melting, the shape, size, internal structure, and order of the crystalline aggregates can also change. For EOCs, several studies[3,18,30] indicate that during crystallization, longer ethylene sequences (higher melting species) crystallize first and form the spherulitic framework for the subsequent crystallization of shorter sequences (lower melting species). Depending on the crystallization conditions, the average size of aggregates of the first forming crystals can be comparable (several hundred nanometers) or larger than the minimum size ($D_{\min} \sim 0.5\ \mu$m) of scatterers whose size and shape can be measured by our SALS instrument. Thus, fluctuations in density and orientation of aggregates with sizes greater than or equal to $D_{\min}$ will dominate the SALS scattering observed. Under these conditions, it is more convenient to describe the scattering of the crystalline aggregates in terms of mean-square fluctuations in the average polarizability ($\langle\eta^2\rangle$) and anisotropy ($\langle\delta^2\rangle$).

The theoretical H_V and V_V invariants defined, as with X-ray scattering, as $Q = \int_0^\infty I(q)q^2\, dq$ have been given for scattering from spherulites.[28] The expression of the H_V invariant is[28,45]

$$Q(H_V) = K\langle\delta^2\rangle = Kx_S(\delta^0_{cr}x_{CS}P_2)^2 \tag{1}$$

where x_S is the volume fraction of spherulites and x_{CS} is the volume fraction of crystals within the spherulites. In eq 1, the amorphous contribution to mean optical polarizability and the form anisotropy are assumed to be negligible. The constant K is $4\pi^6/\lambda^4$ for spherulites.[28] The intrinsic anisotropy of a pure crystal (polyethylene) is δ^0_{cr} and P_2 is a Hermans-type orientation function describing the orientation of crystals with respect to a reference axis. For spherulites, the reference axis is the spherulite radius.

For a system with several types of possible scattering entities (e.g., spherulites and crystalline aggregates with sizes $\geq D_{\min}$), the theoretical H_V and V_V invariants can be generalized as

$$Q(H_V) = K_1\langle\delta^2\rangle = \sum_i K_1^i\, x_S^i(\delta^0_{cr}\, x^i_{CS}\, P^i_2)^2 \tag{2}$$

$$Q(V_V) = K_2\langle\eta^2\rangle + K_3Q(H_V) \tag{3}$$

For each type of scattering entity, x_S^i is the volume fraction of the scattering entity, x^i_{CS} is the volume fraction of crystals within the scattering entity, and P_2^i is the Hermans-type orientation function. The constants K_1, K_1^i, K_2, and K_3 are factors that are products of physical constants that depend on geometry and other quantities kept constant during the experiment. The first term of eq 3 represents the mean-square fluctuations in density of scattering entities. The contribution of this term to the V_V scattering is circularly symmetric. For spherulites, the V_V pattern corresponding to the second term in eq 3 has a 2-fold symmetry with respect to the polarization direction of the polarizer. If the spherulites are space filling ($x_S = 1$), then $\langle\eta^2\rangle = 0$ and $Q(V_V) = K_3Q(H_V)$. The corresponding H_V pattern exhibits 4-fold symmetry with maxima occurring at azimuthal angles, μ, which are odd multiples of 45°. For crystalline aggregates, if the density and orientation fluctuations of the local crystallinity are randomly correlated, both H_V and V_V patterns are circular symmetric.

During melting of space filling[59] spherulites, the crystalline content decreases while the number and size of spherulites and relative orientation of crystals do not change. In order words, P_2 is constant while x_{CS} decreases. According to eq 2, the temperature variation of $Q(H_V)$ should be proportional to $x_{CS}{}^2$. The temperature variation of $Q(V_V)$ (eq 3) is also proportional to $x_{CS}{}^2$ since $Q(V_V) = K_3Q(H_V)$. As the crystallinity decreases, both invariants decrease monotonically. At the final melting temperature of the crystals $Q(V_V) = Q(H_V) = 0$.

As previously discussed, EOCs can form spherulites composed of nanometer or micrometer domains rich in high and lower melting crystals. As these crystals melt, although the crystalline content of the spherulites decreases, the shape and size of micrometer regions that contribute to the overall scattering can change. The refractive index contrast variation (density fluctuations) during melting can be evaluated by examining a two-phase model of crystalline aggregates embedded in an amorphous matrix:

$$\langle\eta^2\rangle = x_S(1 - x_S)\langle(\Delta\alpha)^2\rangle \tag{4}$$

$$\Delta\alpha = (\bar{\alpha}_S - \alpha_0) \tag{5}$$

In eq 5, x_S represents the volume fraction of micrometer aggregates rich in high melting crystals with sizes $\geq D_{\min}$. The average polarizability of these aggregates is $\bar{\alpha}_S$ and that of the matrix (or surrounding amorphous phase) is α_0. The average polarizability can be calculated as

$$\bar{\alpha}_S = \frac{\alpha_r + 2\alpha_t}{3} \tag{6}$$

where α_r and α_t are the radial and tangential polarizabilities of the crystalline aggregates, respectively. Thus, the temperature variation of V_V SALS patterns during melting will show features characteristic of the size and shape of these micrometer crystalline aggregates. The temperature variation of $Q(V_V)$ (eq 3) will not be the same as that for $Q(H_V)$ because $\langle\eta^2\rangle \neq 0$. If

P_2 of each aggregates is constant, the temperature variation of the H_V invariant should be proportional to the square of the crystallinity within each aggregate (eq 2). *This implies that by comparison of both invariants, the spatial organization of different crystalline aggregates formed can be determined*. Below, we show how the proposed generalized scattering equations can be applied to the three main spherulitic morphologies obtained when high and lower melting crystalline aggregates are formed during crystallization.

Case 1. The main assumptions here are that spherulites are volume-filling ($x_S = 1$) and the average size (D_1) of all crystalline aggregates is much less than $D_{\min}$. For this case, eq 2 reduces to eq 1. Although crystals melt at different temperatures, the size and shape of larger regions (spherulites in this case) that contribute to the observed scattering do not change i.e., $\langle\eta^2\rangle = 0$. A monotonic decrease in the H_V and V_V scattering intensities will be observed as crystallinity of the sample decreases.

Case 2. The average size of crystalline aggregates (D_2) is much smaller than the average spherulite size (R_S) but comparable to $D_{\min}$. For this case, eq 2 can be simplified as

$$Q(H_V(T)) = K_1(\delta^0_{cr}P_2)^2\sum_i x^i_S(x^i_{CS}(T))^2; \quad R_S \gg D \geq D_{\min} \tag{7}$$

$Q(H_V)$ will decrease as the crystallinity of each micrometer aggregate decreases. $Q(V_V)$ is given by eqs 3 where x_S and $\bar{\alpha}_S$ (eq 4) now represent the volume fraction and the average polarizability of crystalline aggregates, respectively. In addition, α_r and α_t are polarizabilities along the directions parallel and perpendicular to the optic axis of the crystalline aggregates.

As the lower melting crystals melt initially, there will be a decrease in the average refractive index of domains rich in these crystals. Thus, while the contribution to the overall anisotropic scattering (second term in eq 3) will decrease because of a decrease in crystallinity, there will be a dominating increase in the circularly symmetric V_V scattering (first term in eq 3) arising from the increasing average refractive index difference between the remaining crystalline aggregates and the melted crystals. The scattering intensity will go through a maximum when the contrast between the melted crystals and remaining crystals is the highest. For n types of micrometer aggregates, $n - 1$ maxima corresponding to melting point of each the lower melting aggregates will be observed. The average spherulite size may not change during melting since the refractive index contrast variation does not usually involve the melting of the spherulitic framework until the final stages of melting.

Case 3. Individual spherulites are surrounded by domains rich in very low crystallinity or amorphous material. This morphology belongs to the general class of supermolecular morphologies where nonvolume-filling micrometer lamellar aggregates are surrounded by very low crystallinity or amorphous material. If the low crystallinity lamellar aggregates do not form spherulites, they can form a lamellar base or granular base morphology. For the nonvolume-filling spherulites, SALS patterns obtained at temperatures well below the melting point of all crystals may deviate substantially from that for model spherulites because of excess density fluctuations originating from the refractive index contrast between crystals within spherulites and the surrounding nonspherulitic regions. Initially, inter-spherulitic crystals will melt first. Although the average refractive index in inter-spherulitic regions decreases, there will be a dominating increase in the refractive index difference between remaining crystals, predominantly intraspherulitic crystals and the surrounding melt of newly melted crystals. An intensity maximum will occur when the contrast between the melted crystals and remaining crystals is highest. If the spherulites are composed of domains of high and lower melting crystals with melting points much greater than that of the interspherulitic crystals then there are several possibilities. Both invariants should decrease monotonically to zero (as in case 1**)** as nanometer size intraspherulitic crystalline aggregates melt. If micrometer size intraspherulitic crystalline aggregates are present as in case 2, the V_V invariant would go through a second maximum as the low melting intraspherulitic crystals melt. Both invariants will decrease monotonically to zero when melting is complete. The variation of the H_V invariant near the melting temperature of the inter-spherulitic crystals will depend on whether orientation correlations of these crystals can be resolved. Since the size and shape of larger regions responsible for the light scattering do change during melting, eq 2 cannot be simplified any further. $\sqrt{Q(H_V)}$ will parallel the temperature variation in x_{CS} during melting of each aggregate if the corresponding P^i_2 value is relatively constant. According to eq 2, a sharp or step decrease in $Q(H_V)$ will be occur when crystals in each aggregate melt since $x^i_{CS} = 0$ at the final melting temperature of each crystal species. Thus, for the cases discussed, unique features characteristic of the supermolecular morphology formed during crystallization should be observable in SALS during melting.

In this paper, we use the quantity $(\mathrm{d}\sqrt{Q(H_V(T))}/\mathrm{d}T)$ to monitor the temperature dependence of x_{CS} and the final melting temperatures of crystals. In the absence of absolute intensity measurements, we normalize the invariants with the corresponding values at 30 °C where the scattering entities are volume filling.[29,60] By comparing the shape and size of the SALS patterns and the normalized invariants, $Q(H_V)^N = (Q(H_V(T))/Q(H_V(T = 30\ °C)))$ and $(Q(V_V)^N = Q(V_V(T))/Q(V_V(T = 30\ °C)))$, We determine how the spatial organization of the different crystalline aggregates depend on crystallization conditions.

Models for Analysis of Copolymer Melting

A necessary first step to understanding the crystallization and melting behavior of polymers is to determine the equilibrium melting temperature ($T_m{}^0$), at which an infinitely large crystal melts. Several models[61,62] have been proposed to account for changes in the equilibrium melting temperature of random copolymers as a function of the mole fraction of crystallizable units (x_e). For the complete exclusion of the noncrystallizable comonomer, Flory[61] showed that

$$\frac{1}{T_m{}^c} = \frac{1}{T_m{}^0} - \frac{R}{\Delta H_u}\ln x_e \tag{8}$$

where $T_m{}^0$ is the equilibrium melting point of a perfect (infinitely thick) polyethylene crystal ($T_m{}^0 = 418.7$ K), $T_m{}^c$ is equilibrium melting point of a random copolymer,

ΔH_u is the heat of fusion per mole for a repeat unit (8.284 kJ/mol for C_2H_4 units in polyethylene[3]), and R is the gas constant. According to eq 8, $T_m{}^c$ should not depend on the nature of the counit as long as the comomoner is noncrystallizable and completely excluded from the crystal lattice. For the case where the noncrystallizable comomoner is uniformly included in the crystal, Sanchez and Eby[62] showed that

$$T_m{}^c = T_m{}^0\left(1 - \frac{\epsilon(1 - x_e)}{\Delta H_u}\right) \tag{9}$$

where ϵ is the excess free energy of the defect created by incorporating units of noncrystallizable comonomers into crystals. Theoretical estimates[63] of ϵ for isolated defects such as a kink or Renecker defect range from 35.59 to 56.62 kJ/mol while values ranging from 23.0 to 54.0 kJ/mol have been predicted[63] for branched molecules. From eqs 8 and 9, $T_m{}^c$ is defined for melting of the thickest possible crystals with dimensions approaching infinity. The amount of such crystals is so small that $T_m{}^c$ is impossible to measure, even if the thick equilibrium crystals are present.[19,62−66]

The Gibbs−Thomson relation for the melting of thin crystals is the most reliable means for estimating the equilibrium melting temperature ($T_m{}^e$) of a lamellar crystal with large lateral dimensions and infinite thickness. This approach utilizes the correlation between lamellar thickness and crystal stability. The experimentally observed melting temperature (T_m) of lamellar crystals can be written as

$$T_m = T_m{}^e\left(1 - \frac{2\sigma_e}{l\Delta H_v}\right) \tag{10}$$

where l is the lamellar thickness, σ_e is the end (fold) surface free energy, ΔH_v is the heat of fusion per unit volume for the perfect crystal, and $T_m{}^e$ represents the melting point of an infinitely thick crystal. $T_m{}^e$ is estimated by extrapolation of T_m vs $1/l$ data to $1/l = 0$. The extrapolated value is compared to theoretical values for $T_m{}^0$.[67] For copolymers, the equilibrium melting temperature of the infinitely thick crystals is $T_m{}^c$, thus replacing $T_m{}^e$ with $T_m{}^c$ in eq 10 gives

$$T_m = T_m{}^c\left(1 - \frac{2\sigma_e}{l\Delta H_v}\right) \tag{11}$$

This modified Gibbs−Thomson relation was first proposed by Sanchez and Eby.[62] The equation is correct when the melt composition equals to x_e, i.e., when melting is virtually complete. Thus, this equation provides a relationship between the final melting temperature ($T_m{}^f$) and crystal thickness (l_f) at the final stages of melting. For hydrogenated polybutadienes (HPB's), model random copolymers of ethylene and 1-butene characterized by narrow molecular mass distributions ($M_w/M_n < 1.1$) and compositional homogeneity, it has been shown[18−20] that thickest crystals with observable populations melt at a final melting temperature which is below $T_m{}^c$. $T_m{}^f$ decreases monotonically with increasing branch content, as expected from eq 11. Such trends have also been observed for both heterogeneous and homogeneous EOCs.[15,39,68]

In this paper, we determine l_f from SAXS the intensity profiles obtained during the final stages of melting. At the final stages of melting, SAXS profiles should be characteristic of isolated crystals and can be described by Guinier's law for isolated domains at high dilution and for randomly oriented thin platelets.[47,69] The intensity variations are given by[70]

$$I(q,t) \propto \exp\left[-\frac{R_g{}^2q^2}{3}\right] \tag{12}$$

$$I(q,t) \propto q^{-2}\exp\left[-\frac{l_g{}^2q^2}{12}\right] \tag{13}$$

where R_g is the radius of gyration of the isolated domain and l_g is the thickness of the platelet. During the final stages of melting, a Guinier plot should give a domain size similar to the crystal thickness of the initial crystals formed during crystallization,[47] i.e., R_g (or l_g) $= l_f$ at $T_m{}^f$. Using l_f from SAXS and $T_m{}^f$ values obtained from SALS, we examine the validity of eqs 8 and 9 for describing of the equilibrium melting temperature of the copolymer studied.

Results and Discussion

Supermolecular Morphology. Despite the compelling evidence for associating multiple DSC melting peaks of EOCs with separate morphological entities,[25,42,71] a number of questions remain unanswered: How does crystallization temperature (T_c) and time affect the spatial organization of these morphological units? Are all DSC peaks associated with distinct supermolecular structures?

Figure 1 shows typical DSC melting curves obtained for EH064 samples rapidly cooled to room temperature from the melt (160 °C) and after isothermal crystallization at 81, 88, and 103 °C. Near 40 °C, a small broad endotherm whose shape and position is not sensitive to crystallization conditions is observed. This peak has been observed for other polyolefins and has been attributed to annealing at room temperature of highly branched chains crystallized on cooling to room temperature.[2,3] For samples crystallized at temperatures $\gg$ room temperature, no effect of crystallization conditions on this peak is observed because polymer chains crystallizing near room temperature are in the molten state. Above 40 °C, a single broad melting endotherm with a peak melting temperature ($T_m{}^p = 94$ °C) is observed for the quenched sample (Figure 1a). This observation is consistent with the crystallization of polymer chains with a random ethylene sequence distribution. Under isothermal crystallization conditions, multiple melting endotherms obtained for *ran*-EOCs have been attributed to the distribution of ethylene sequences or chain segments that can participate in the crystallization and annealing at a particular temperature.[1,3,18,72,73] Such multiple melting behavior cannot be explained by a mechanism of melting−recrystallization-remelting during heating[1,3,18] because the melting behavior is independent of heating rate. When EH064 samples are isothermally crystallized at temperatures below $T_m{}^p =$ 94 °C, additional melting endotherms are observed. For example in Figure 1c, the highest $T_m{}^{p,1} = 98$ °C and lower $T_m{}^{p,2} = 92$ °C melting crystals correspond to lamellar crystals formed from the longest ethylene sequences and smaller crystals formed from shorter sequences during isothermal crystallization at 88 °C, respectively. Shorter chain segments that crystallize during the subsequent rapid cooling to room temperature melt at $T_m{}^{p,3} \approx 81$ °C. These crystals are thinner

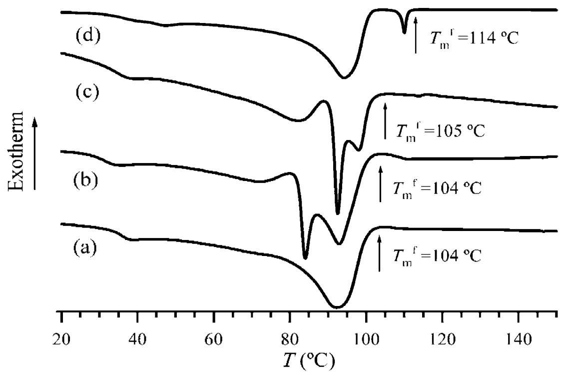

Figure 1. DSC melting curves for EH064 samples rapidly cooled to room temperature after (a) melting at 160 °C for 10 min and isothermal crystallization at (b) 81 °C for 1 h, (c) 88 °C for 1 h, and (d) 103 °C for 72 h.

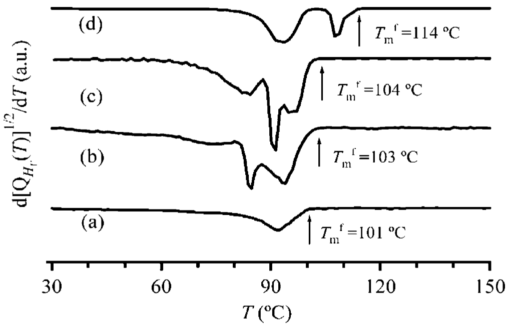

Figure 2. SALS ($\mathrm{d}\sqrt{Q_{H_V}(T)}/\mathrm{d}T$) melting curves for EH064 samples rapidly cooled to room temperature after (a) melting at 160 °C for 10 min and isothermal crystallization at (b) 81 °C for 1 h, (c) 88 °C for 1 h, and (d) 103 °C for 72 h.

and may organize to form micrometer regions within or outside spherulites. As T_c is increased, the area of the melting endotherm for crystals that form on rapid cooling to room temperature increases and the shape of the high melting endotherm for lamellar crystals becomes narrower, indicating that the number of ethylene sequences that can crystallize isothermally decreases with increasing T_c (Figure 2b–d). The final melting temperature ($T_m{}^{f,DSC}$) of the crystals is relatively constant at large undercoolings ($T_c < T_m{}^p = 94$ °C) and increases to a limiting value of 114 °C for higher T_c's and long (72 h) crystallization times. The results shown in Figure 1 are typical for *ran*-EOCs.

Figure 2 shows SALS ($\mathrm{d}\sqrt{Q(H_V(T))}/\mathrm{d}T$) melting curves for EH064 samples with the same thermal history as the samples shown in Figure 1. Because SALS melting curves obtained at 10 °C/min (not shown in the paper) are identical to the curves shown in Figure 2, these melting curves can be directly compared with the DSC melting curves (Figure 1). For the isothermally crystallized samples, values for the final melting temperature from H_V SALS are identical to the corresponding DSC values within the uncertainty (±1 °C) of the measurements. Above 40 °C, the number and general shape of peaks observed are the same for corresponding ($\mathrm{d}\sqrt{Q(H_V(T))}/\mathrm{d}T$) and DSC melting curves. From DSC, crystals that melt near room temperature (Figure 1) are either incorporated into the superstructures or located at their boundaries since no corresponding peak is observed in ($\mathrm{d}\sqrt{Q(H_V(T))}/\mathrm{d}T$) curves (Figure 2). It is also possible that the scattering from the orientation correlations of aggregates of these crystals occurs at angles much larger ($q \gg 2.4\ \mu\mathrm{m}^{-1}$) than the accessible range for our SALS measurements. Even if superstructures of these crystals are present, scattering arising from orientation fluctuations may be too low to be resolved by H_V SALS. In subsequent discussions we will show that the density fluctuations from these crystalline aggregates can be measured by V_V SALS.

A distinctive feature of the melting peaks for the sample crystallized at 103 °C (Figures 1d and 2d) is that the relative peak area (or height) of the highest melting crystal population ($T_m{}^{p,1} = 110$ °C) is much larger in the ($\mathrm{d}\sqrt{Q(H_V(T))}/\mathrm{d}T$) curve than in the corresponding DSC melting curve. The temperature variation of DSC melting curves is temperature variation in crystallinity,w_c, defined as $w_c = \sum_i x_S^i\, x_{CS}^i$. If P_2 is assumed to be constant during melting, then the temperature variation of $\sqrt{Q(H_V)}$ is proportional to $\sum_i \sqrt{x_S^i}\, x_{CS}^i$ (eq 7). For the samples crystallized at 81 and 88 °C, the relative peak areas of the $T_m{}^{p,1}$, $T_m{}^{p,2}$, and $T_m{}^{p,3}$ crystal populations in DSC and SALS are similar suggesting that the observed temperature variation in w_c and $\sqrt{Q(H_V)}$ is independent of x_S and is proportional to the temperature variation of the crystallinity of each aggregate. This implies that average size of each crystalline aggregate is smaller than the average spherulite size ($R_S = 4.1 \pm 0.2\ \mu$m, determined by $4.1/q_{\max}$, with $q_{\max}$ being the scattering vector at which the maximum of H_V scattering at $\mu = 45°$ occurs). For the sample crystallized at 103 °C, the $T_m{}^{p,1} = 110$ °C and $T_m{}^{p,2} = 95$ °C crystal populations (Figures 1d and 2d) arise from micrometer aggregates of these crystals because the peak corresponding to $T_m{}^{p,1}$ crystals will be much larger in $\sqrt{Q(H_V)}$ than in DSC if $x_S{}^1 \ll 1$. It must be noted that when all crystals within a given superstructure have melted, the corresponding $x_S^i\, x_{CS}^i$ term vanishes. At higher temperatures, $\sum x_S^i$ would be less than 1. Whether the average size of $T_m{}^{p,1}$ crystalline aggregates is comparable to $D_{\min}$ (case 2) or larger than $D_{\min}$ (case 3) can be deduced by comparing calculated DSC and H_V SALS melting curves (($\mathrm{d}w_c/\mathrm{d}T$) and ($\mathrm{d}\sqrt{Q(H_V(T))}/\mathrm{d}T$) for model aggregates of high and lower melting crystals to our corresponding experimental curves in Figures 1 and 2.

Model calculations of melting behavior of high and low melting crystalline aggregates for case 2 and case 3 are shown in Figure 3. For both cases, the relative height (or area) of the melting peak corresponding to the high melting crystals is larger in the ($\mathrm{d}\sqrt{Q(H_V(T))}/\mathrm{d}T$) curve than in the ($\mathrm{d}w_c/\mathrm{d}T$) curve. This trend is relatively independent of the actual values of x_S and x_{CS} used in the calculation. For calculation of case 2 (Figure 3a), we used $x_{CS}^1 = 0.1$ and $x_{CS}^2 = 0.2$ for the initial crystallinities of the high and low melting species, respectively. During melting, spherulites remain volume-filling ($x_S = 1$) and the crystallinities decrease at the respective melting temperatures. For calculation of case 3 (Figure 3b), the volume fraction of aggregates of high and low melting crystals are $x_S^1 = 0.2$ and $x_S^2 = 0.8$, respectively. For both species, $x_{CS}^1 = x_{CS}^2 = 0.3$. The values of x_{CS} used for these calculations are representative of the values determined from SAXS.[74] For case 2, the relative peak areas of the populations from SALS and DSC are comparable while that for the high melting crystal is much smaller from DSC for case 3 suggesting that for the sample crystal-

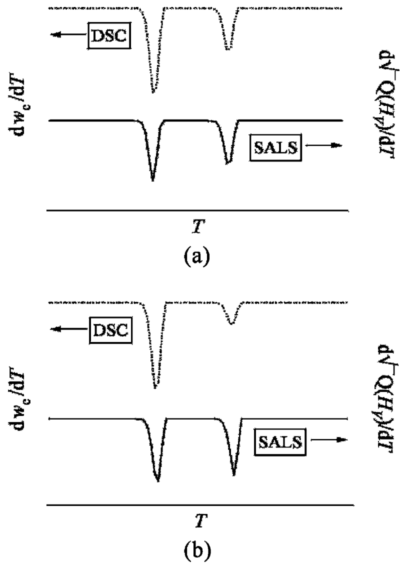

Figure 3. Calculated SALS ($d\sqrt{Q_{H_V}(T)}/dT$) and DSC melting curves for (a) case 2, $x_S = 1$, x_{CS} (lower melting) = 0.2, x_{CS} (higher melting) = 0.1; (b) case 3, $x_{CS} = 0.3$, x_S (lower melting) = 0.8, x_S (higher melting) = 0.2;

lized at 103 °C, aggregates of the $T_m^{p,1}$ = 110 °C and $T_m^{p,2}$ = 95 °C crystal populations observed are much larger than D_{min}. These crystals are within spherulites surrounded by domains rich in near room temperature crystals.

Our calculations indicate that the differences between the experimental ($d\sqrt{Q(H_V(T))}/dT$) and DSC melting curves are dominated by differences in the relative size of the crystalline aggregates formed under a given crystallization condition. This result suggests that variation of P_2 during melting may not be very important. It is possible that P_2 does not vary significantly during melting because the relative orientation of intraspherulitic low melting crystals is determined by the high melting crystals that are formed first during crystallization.[19,30] In addition, the contribution of relative orientation of the latter forming crystals to P_2 may be small. As mentioned earlier, the orientation fluctuations of crystals that melt below 40 °C may be too low to be resolved by H_V SALS. The variation in refractive index as these crystals melt should give the distinctive features in V_V scattering. Similarly, variations in the refractive index during melting of nanometer and micrometer aggregates of intraspherulitic crystals should also give unique features in the V_V scattering. Hence, although a comparison of experimental data and model calculations on the temperature variation of ($d\sqrt{Q(H_V(T))}/dT$) and DSC melting curves can be used to predict the supermolecular morphology formed for a given crystallization condition, one needs to consider the temperature variation of the H_V and V_V SALS patterns and the corresponding invariants to determine (a) how many crystal populations are present and (b) if the crystal populations observed are large enough to be classified as distinct superstructures.

Figures 4 and 5 show typical H_V and V_V patterns during melting of EH064 samples with the same thermal history as samples shown in Figures 1 and 2. For samples crystallized at temperatures below T_m^p = 94 °C the room temperature (30 °C) H_V (Figure 4a–c) and V_V (Figure 5a–c) patterns are typical for volume-filling well-developed spherulites with $R_S = 4.1 \pm 0.2$ μm. These results are consistent with the POM's obtained for these samples (Figure 6a–c). When samples are crystallized above T_m^p = 94 °C, the room temperature H_V (Figure 4d) and V_V (Figure 5d) patterns indicate that the spherulites are either poorly developed or nonvolume-filling. The corresponding POM (Figure 6d) indicates that the morphology is composed of nonvolume-filling spherulites surrounded by micrometer domains rich in very low birefringent crystalline aggregates. The birefringence of the interspherulitic crystals is too low to be resolved by POM.

During melting of the sample rapidly cooled directly from the melt (160 °C), the size and shape of the H_V

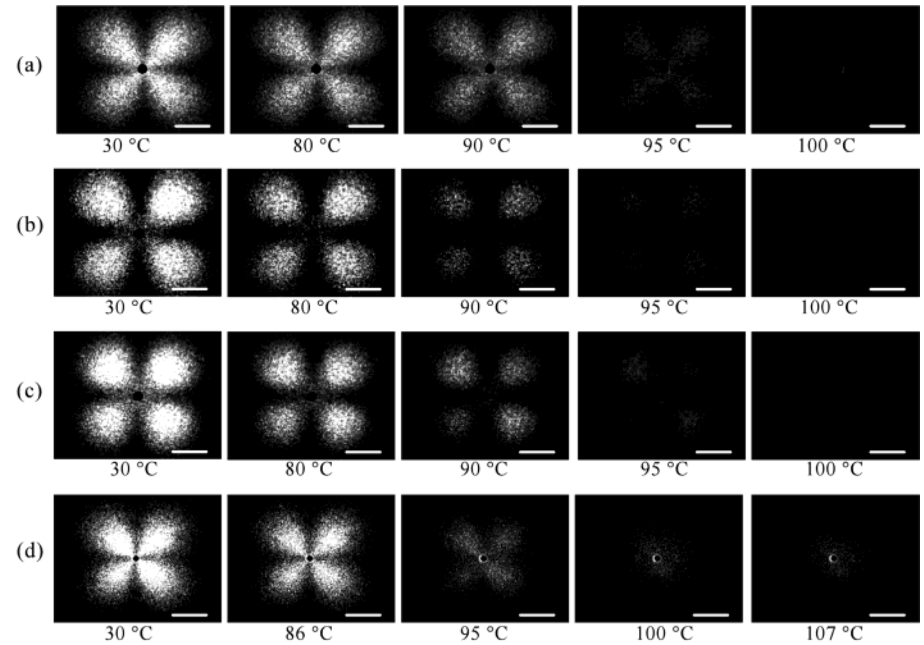

Figure 4. Changes in SALS H_V patterns during melting of EH064 samples rapidly cooled to room temperature after (a) melting at 160 °C for 10 min and isothermal crystallization at (b) 81 °C for 1 h, (c) 88 °C for 1 h, and (d) 103 °C for 72 h. The scale bar is equivalent to a scattering angle $2\theta = 5°$.

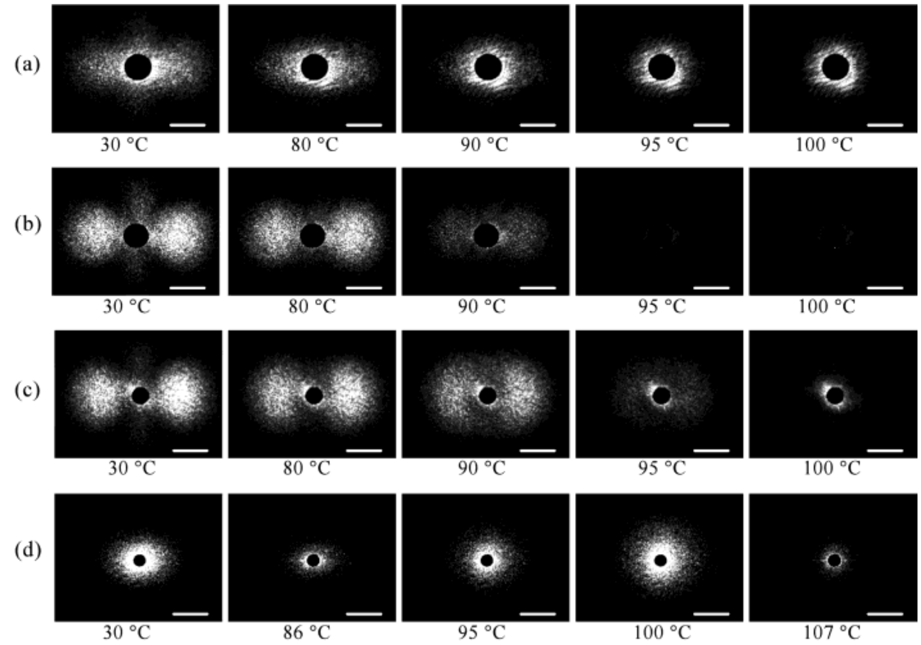

Figure 5. Changes in SALS V_V patterns during melting of EH064 samples rapidly cooled to room temperature after (a) melting at 160 °C for 10 min and isothermal crystallization at (b) 81 °C for 1 h, (c) 88 °C for 1 h, and (d) 103 °C for 72 h. The scale bar is equivalent to a scattering angle $2\theta = 5°$.

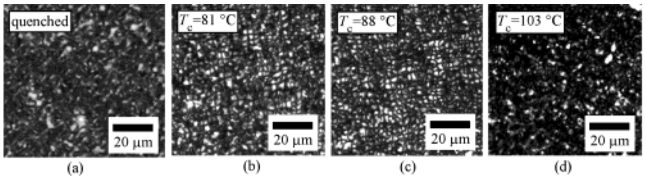

Figure 6. Polarized optical micrographs obtained at room temperature for the EH064 samples rapidly cooled to room temperature after (a) melting at 160 °C for 10 min and isothermal crystallization at (b) 81 °C for 1 h, (c) 88 °C for 1 h, and (d) 103 °C for 72 h.

patterns (Figure 4a) do not change, suggesting that x_S and P_2 remain constant while x_{CS} decreases. This observation also implies that although crystals melt at different temperatures (Figure 1a), the size and shape of larger regions responsible for light scattering do not change significantly such that the intensity of the H_V patterns (Figure 4a) decreases monotonically without a significant change in the average size and shape. The normalized invariants also show that no significant excess density fluctuations originating from the refractive index contrast variation develop during melting (Figure 7a). These observations indicate that the correlation distance between similar crystalline aggregates is much smaller than D_{min}, which is in agreement with case 1. Crystals within the spherulites may be segregated at the lamellar level as previously proposed for EOCs crystallized under similar conditions.[5,60] The H_V and V_V SALS patterns observed for the sample crystallized at 81 °C (Figures 4 and 5) are similar to the ones observed for the sample rapidly cooled directly from the melt, indicating that that the correlation distance between the crystalline aggregates is also smaller than D_{min}. In the corresponding V_V invariant (Figure 7b), the slight excess density fluctuations observed above 94 °C suggest that the average correlation distance for crystals with $T_m > 94$ °C is greater than the Rayleigh limit (32 nm) but less than D_{min} since clear features consistent with the size and shape of these regions are not visible in the corresponding V_V patterns.

As T_c is increased further, pronounced changes in the shape of the SALS patterns (Figures 4 and 5) and invariants (Figure 7) are observed during melting. These changes are consistent with an increase in the average correlation distance between similar crystalline aggregates with increasing T_c such that the size and shape of the resulting large regions ($D > D_{min}$) with differing refractive index contrast ($\Delta\alpha$) and orientational order (P_2) contribute to the observed scattering. The dominating increase in the isotropic V_V scattering (Figure 5) and excess density fluctuations (Figure 7) arises from the increasing refractive index difference between the remaining crystalline aggregates and domains rich in melted crystals. Maxima in the V_V invariant and intensity of the corresponding patterns would occur near the T_m^f of the lower melting crystals, because at this temperature the contrast between melted and remaining crystalline aggregates is the highest. For the sample crystallized at 103 °C, the V_V invariant goes through maxima near 60 and 100 °C and then decreases monotonically to zero at 114 °C (Figure 7d). The first maximum occurs while the average spherulite size from H_V is constant, suggesting that the observed density contrast variation is from the melting of crystals surrounding the spherulites. For the V_V maximum at 100 °C, there is a corresponding step decrease in the H_V invariant consistent with the melting of intraspherulitic crystalline aggregates with $D_{min} \ll D \sim R_S$. These crystals are formed during the rapid cooling from T_c to room temperature and R_S is determined by the $T_m^{p,1} = 110$ °C crystals that form the spherulitic framework during isothermal crystallization at 103 °C. As the $T_m^{p,1} = 110$ °C crystals melt, both invariants decreases monotonically to zero at the $T_m^f = 114$ °C. These results indicate that the three melting endotherms observed from DSC (Figure 1d) correspond to micrometer aggregates of three distinct morphological units with $T_m^{f,1} = 114$ °C, $T_m^{f,2} = 110$ °C, and $T_m^{f,1} \approx 60$ °C. The orientational order of the lowest melting species is too low to be resolved with H_V SALS, but the refractive index contrast variation during melting of

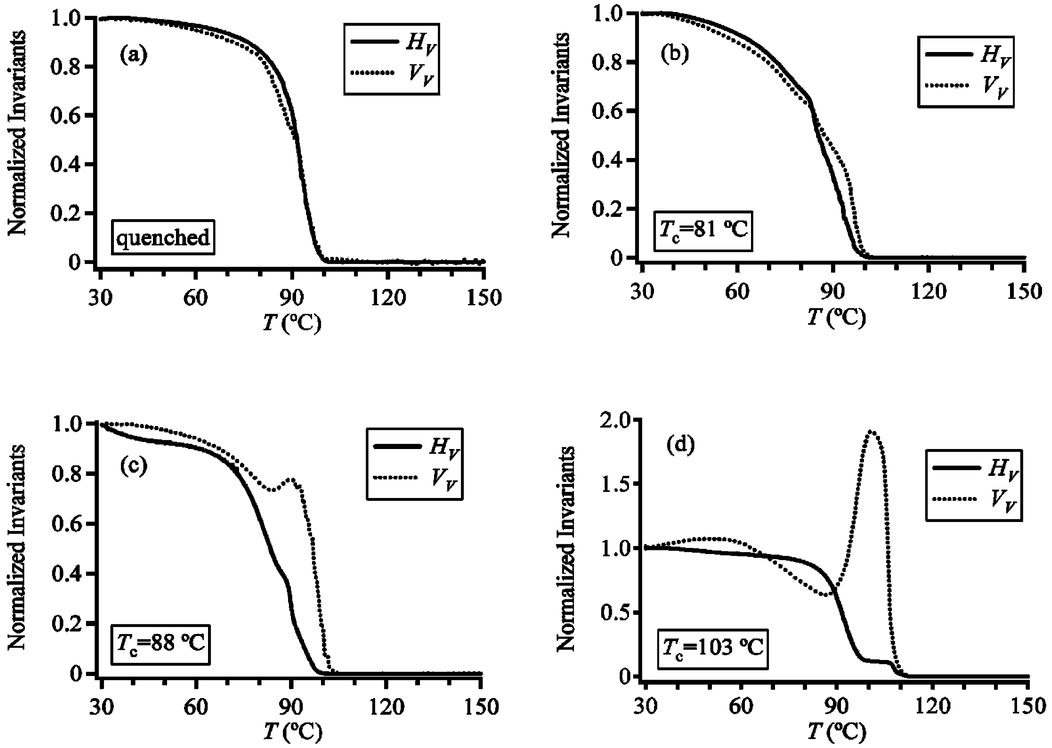

Figure 7. Changes in normalized V_V invariants (dotted line) and normalized H_V invariants (solid line)) during melting of the EH064 samples rapidly cooled to room temperature after (a) melting at 160 °C for 10 min and isothermal crystallization at (b) 81 °C for 1 h, (c) 88 °C for 1 h, and (d) 103 °C for 72 h.

these species is detected by V_V SALS (Figure 7d). These observations are consistent with predicted scattering during melting of case 3 spherulites embedded in a matrix of low crystallinity material.

For the sample crystallized at 88 °C, the multiple DSC melting peaks (Figure 1c) observed correspond to crystalline aggregates within volume-filling spherulites. Because the size and shape of the H_V patterns do not change during melting, these aggregates are smaller than the average spherulite size. Aggregates of $T_m^{p,1}$ and $T_m^{p,2}$ crystals are larger than D_{min} since the size and shape of the corresponding V_V patterns (Figure 5c) change during melting of these crystals, while aggregates of $T_m^{p,3}$ and the near room temperature crystals are smaller than D_{min}. The melting behavior of the sample crystallized at 88 °C is consistent with case 2.

In the preceding discussion, we have shown that the spatial organization of crystals can be evaluated by comparing the normalized H_V and V_V invariants. Separate H_V and V_V measurements are necessary to perform such a comparison. Because most polymers do not absorb visible light, the measurement of light transmitted by a sample, which is not analyzed, can also provide information about the total scattering. The turbidity (τ) is a measure of the total scattering and is defined by the relation

$$\tau = \frac{1}{d}\ln\left[\frac{100}{\%\ T_T}\right] \tag{14}$$

where T_T is the fraction of incident light transmitted by a sample of thickness d. Variations in $Q(V_V)$ and τ (or % T_T) during crystallization and melting may parallel each other if scattering from crystalline aggregates falls off sufficiently with angle and if the temperature variation of $Q(H_V)$ is much smaller than that of $Q(V_V)$.[28,30,38] As shown in Figure 8, the temperature variation of τ is indeed parallel to $Q(V_V)$ for the EH064 samples studied. Therefore, the temperature variation of the excess density fluctuations can be examined by comparing the normalized H_V invariant and the normalized turbidity. Both quantities can be obtained in one combined measurement of H_V scattering and transmitted light. It should be noted that for the EH064 samples the temperature variation of total scattering is dominated by the temperature variation of the scattering arising from density fluctuations, thus τ parallels $Q(V_V)$. For systems where orientation fluctuations dominates the total scattering, the temperature variation of turbidity might not parallel that of $Q(V_V)$. In such cases, the turbidity reflects variation of both $Q(V_V)$ and $Q(H_V)$.[75]

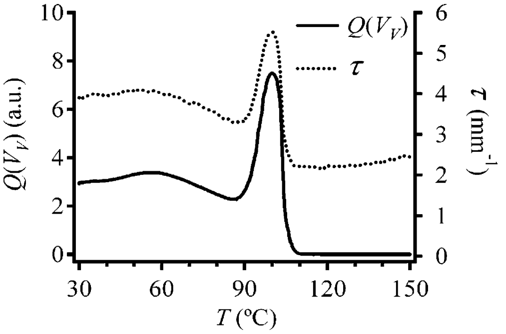

Figure 8. Comparison between changes of $Q(V_V)$ and turbidity (τ) during melting of EH064 samples rapidly cooled to room temperature after isothermal crystallization at 100 °C for 18 h.

Lamellar Morphology. The crystallization of linear polyethylene (LPE) has been shown to occur in stages which reflect the evolution of isolated crystals to lamellar aggregates.[69,76] Such phenomenon is also observed during the crystallization of EOCs with very low branch

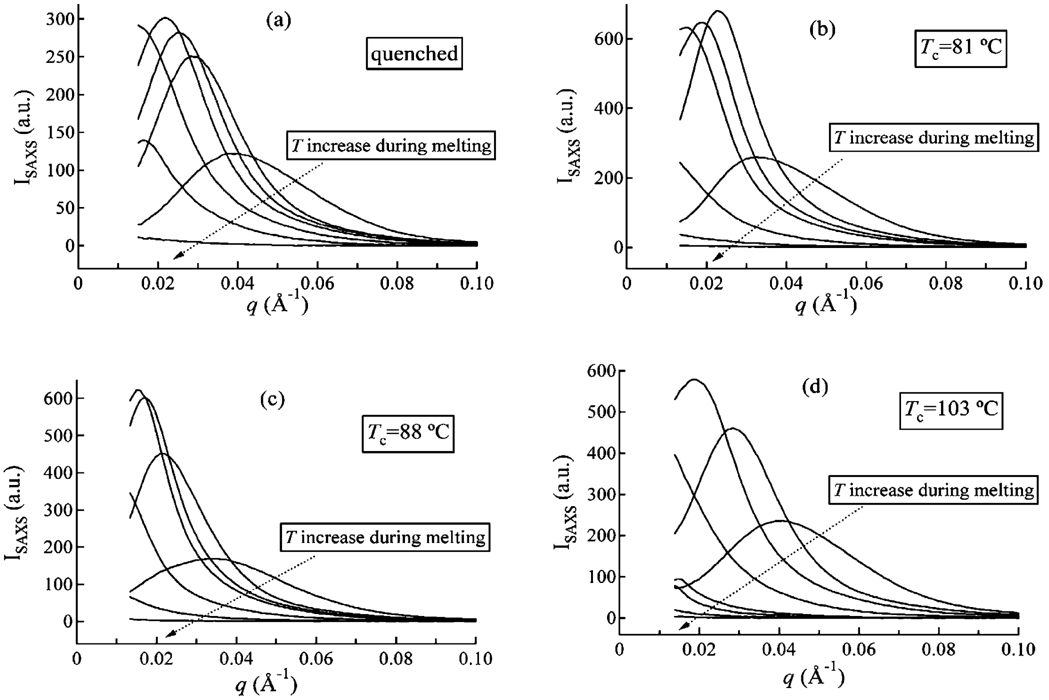

Figure 9. Evolution of SAXS during melting of the EH064 samples rapidly cooled to room temperature after (a) melting at 160 °C for 10 min and (b) isothermal crystallization at 81 °C for 1 h, (c) isothermal crystallization at 88 °C for 1 h, and (d) isothermal crystallization at 103 °C for 72 h. The temperatures shown in parts a–c are 32, 80, 85, 90, 95, 100, and 105 °C; the temperatures shown in part d are 32, 80, 90, 95, 100, 105, 109, and 113 °C.

content.[30] At sufficiently high crystallization temperatures ($T_c \gg T_m^p = 94$ °C) the shape of the H_V (Figure 4d) and V_V (Figure 5d) SALS patterns for EH064 evolve from one characteristic of nonvolume-filling spherulites to isolated crystalline aggregates. SAXS $I(q)$ vs q profiles (Figure 9d) for a sample crystallized under the same conditions evolve from peaked to monotonic curves indicating that isolated lamellae are present at the end of melting.[9,77] These changes are consistent with the reverse of crystallization that starts with the formation of isolated lamellar crystals.[30,69] Since these changes are also observed for the samples crystallized at lower temperatures (Figure 9a–c), we can conclude that the development of the lamellar morphology is similar at all crystallization temperatures. Below 70 °C, where reliable estimates for SAXS morphological variables are obtained, average values of the long period, crystalline and amorphous thicknesses for the crystallization conditions studied are 127 ± 7, 43 ± 3, and 85 ± 6 Å, respectively. The variation of these variables during melting is also independent of crystallization conditions. The marked differences observed in the intensity variation of the SALS patterns and invariants for samples crystallized are not evident from SAXS because there is a general mechanism for the development of the lamellar morphology. For SALS, the characteristics of low melting crystalline aggregates depend on the nature of higher melting aggregates formed at a given temperature. This means that both SAXS and SALS crystallization and melting measurements are necessary to understand how crystallization conditions determine the nanometer to micrometer spatial arrangement of crystals. In effect, the development of crystallization[5] and melting[50] mechanisms that correctly predict the hierarchal spatial arrangement of crystals may require detailed quantitative SAXS and SALS crystallization and melting studies. For higher branched EOCs, our preliminary results indicate that the H_V and V_V scattering during melting show features that depend on the branch content. These results indicate that SALS is a promising tool for understanding how chemical microstructure and crystallization conditions determine the supermolecular morphology of EOCs.

Determining Equilibrium Melting Temperature. The variation of the final melting temperature T_m^f of the crystals with T_c can provide insight into the characteristics of the initial crystals formed during crystallization.[19,63] Figure 10 shows the T_m^f values determined from the temperature variation of $Q(H_V)$ and DSC endotherms during melting of EH064 samples isothermally crystallized at temperatures ranging from 81 to 110 °C for different times. In subsequent discussions, we will refer to the final melting temperatures from H_V SALS and DSC as T_m^{f,H_V} and $T_m^{f,DSC}$ respectively. The T_m^f values determined from $Q(V_V)$ (not shown in the paper) are the same (within ±1 °C) as that from $Q(H_V)$.At $T_c > T_m^p = 94$ °C, T_m^{f,H_V} and $T_m^{f,DSC}$ increase with temperature to a limiting value of 114 ± 1 °C for sufficiently long crystallization times (several days) and high temperatures (>100 °C) indicating that SALS can be reliably used to determine T_m^f under these crystallization conditions. For shorter crystallization times, T_m^{f,H_V} decreases with temperature while that from DSC is relatively constant. When $T_c < T_m^p$, T_m^{f,H_V} and $T_m^{f,DSC}$ are relatively independent of crystallization conditions. These observations can be rationalized if one considers the sensitivity of each technique to the size and perfection of crystals and the corresponding aggregates formed under a given crystallization condition.

The integrated SAXS intensity and integrated area under crystalline reflections from WAXS during melting can be used to determine T_m^f of lamellar crystals directly.[31,47,69] $T_m^{f,SAXS}$and $T_m^{f,WAXS}$ values are shown in Figure 11. For short to moderate crystallization times (1–18 h) $T_m^{f,SAXS}$and $T_m^{f,WAXS}$are relatively independent of T_c within the uncertainty of the measurements. The

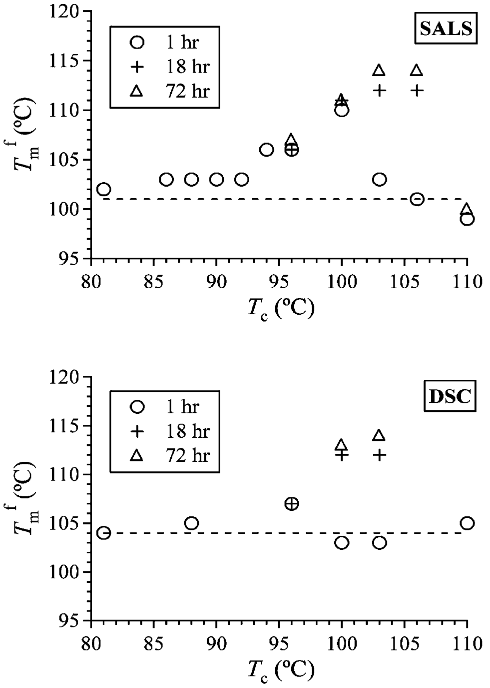

Figure 10. T_m^f values obtained from H_V SALS and DSC melting measurements as a function of T_c for the indicated crystallization times. The dotted line is for the T_m^f value obtained from the EH064 sample rapidly cooled to room temperature after melting at 160 °C for 10 min. The uncertainty in T_m^f is ±1 °C.

overall variation of $T_m^{f,SAXS}$ and $T_m^{f,WAXS}$ with T_c is also a function of the size and perfection of the highest melting crystals and the sensitivity of each technique. Our results indicate that the sensitivity of SAXS and WAXS is about the same if a two-dimensional detector is used. This finding is in contrast to results obtained from one-dimensional detectors which suggest that WAXS is less sensitive to detecting crystals than SAXS.[31] On the other hand, SALS is the most sensitive scattering technique for measuring the dependence of T_m^f on T_c over a wide range of T_c's and at moderate crystallization times. For short crystallization times, the interpretation of results from any scattering measurement during crystallization or melting will strongly depend on the sensitivity of the technique used. However at sufficiently high T_c and long crystallization times, all techniques (DSC, SAXS, WAXS, and H_V SALS) can be used to reliably determine the final melting temperature of EOC crystals since the same limiting value for T_m^f (T_m^f = 114 °C) is obtained from all techniques.

The thickness of the final melting crystals (l_f) was determined from the SAXS intensity profiles for the EH064 sample crystallized at 103 °C for 72 h. A typical Guinier plot using eq 12 for SAXS intensity profiles obtained during the final stage of melting are shown in Figure 12. At these temperatures, a dense domain with an average size (R_g = 11 ± 2 nm) is obtained. Our attempts to fit these intensity profiles to eq 13 failed. In contrast to LPE,[47] no linear relationship between $\ln(Iq^2)$ and q^2 in the low q was obtained for the EH064 final melting crystals. This is because the lateral dimensions of these crystalline domains are smaller than that in LPE. This reduction in lateral dimensions is to be expected for the crystallization of ethylene sequences/units in the presences of short chain branches.

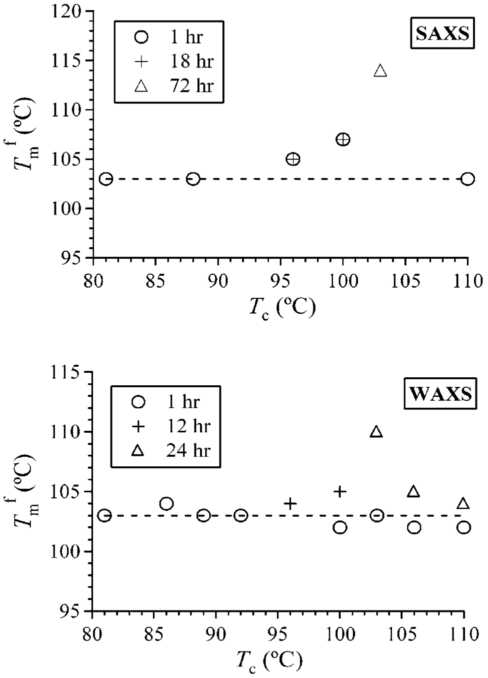

Figure 11. T_m^f values obtained from SAXS and WAXS melting measurements as a function of T_c for the indicated crystallization times. The dotted line shown is for the T_m^f value obtained from the EH064 sample rapidly cooled to room temperature after melting at 160 °C for 10 min. The uncertainty in T_m^f is ±2 °C.

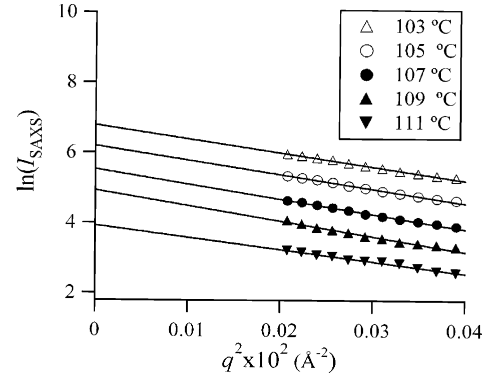

Figure 12. Guinier plots at various temperatures during the final stages of melting of an EH064 sample rapidly cooled to room temperature after isothermal crystallization at 103 °C for 72 h. The plots are offset for better visualization. Lines represent fits to the data points using eq 12.

Since a Guinier plot interpreted in terms of scattering by monolayer crystals should give a domain size similar to that found for the crystal thickness at the same temperature, we use the R_g value obtained from the Guinier plots (Figure 12) as an estimate for l_f.

Using standard thermodynamic values for polyethylene crystals (T_m^0 = 418.7 K, σ_e = 90 mJ/m^2, ΔH_v = 285 mJ/m^3, ΔH_u = 8.284 kJ/mol, ϵ = 23.0 kJ/mol), the predicted T_m^c values for the random copolymer containing 6.4% comonomer are 134 °C and 71 °C for complete exclusion (eq 8) and inclusion (eq 9) of comonomer units in the crystal, respectively. With the experimentally determined values of T_m^f (114 ± 1 °C) and l_f (11 ± 2 nm), T_m^c can also be calculated from the modified Gibbs−Thomson equation (eq 11). The result, T_m^c = 136 ± 2 °C, is consistent with the value ($T_m^{c,Flory}$ = 134 °C) predicted from Flory's equilibrium theory of melting (eq 8), indicating that for the copolymer studied all defects will be excluded if the sample is crystallized at sufficiently high temperatures and long times. Crystal thicknesses determined from room-temperature SAXS curves give much lower thicknesses (~4 nm) which can lead one to conclude that defects are partially included in the crystal for this conomoner concentration as previously proposed.[63] At this time, we are not sure if EOCs with higher comonomer contents (>6.4 mol %) can be crystallized under conditions which allow defects to be completely excluded from the crystal. We are currently investigating this possibility.

Conclusions

For the copolymer studied, the melting behavior of samples crystallized under different conditions is well represented by the generalized SALS model proposed. Our results demonstrate that SALS can be used to accurately measure T_m^f of crystals and characterize the structure and spatial arrangement of their aggregates. More importantly, we show that SALS can be used to understand the impact of nanometer to micrometer aggregates of different crystals on the supermolecular morphology. If a DSC/H_V SALS approach is used, then model calculations are necessary to determine the specific supermolecular morphology formed. On the other hand, by comparing H_V and V_V patterns and invariants, the refractive index contrast variation during melting of nanometer and micrometer crystalline aggregates provides a direct means for characterizing the structure and spatial arrangement crystals. Thus, SALS can be used to understand and provide a quantitative description of how crystallization conditions affect the supermolecular organization of copolymers of ethylene and α-olefins and other semicrystalline polymers.

Acknowledgment. The SALS instrument used for this work was developed with National Science Foundation support under NSF DMR-0108976. We acknowledge the "2001 Mettler-Toledo Thermal Analysis Educational Grant" for providing the DSC instrument. SAXS and WAXS experiments were carried out at the National Synchrotron Light Source, Brookhaven National Laboratory, which is supported by the U.S. Department of Energy, Division of Materials Sciences and Division of Chemical Sciences. The authors would like to thank ExxonMobil for use of beamline X10A for measurements. We would also like to thank Steve Bennett for helping with the synchrotron X-ray setup and Dr. D. J. Lohse (ExxonMobil) for providing the copolymer studied. Many helpful discussions of our results with Dr. R. Kolb (ExxonMobil) and Prof. V. B. F. Mathot (DSM Research, Netherlands) are gratefully acknowledged.

References and Notes

(1) Alamo, R. G.; Mandelkern, L. *Thermochim. Acta* **1994**, *238*, 155−201.
(2) Kim, M. H.; Phillips, P. J. *J. Appl. Polym. Sci.* **1998**, *70*, 1893−1905.
(3) Alizadeh, A.; Richardson, L.; Xu, J.; McCartney, S.; Marand, H.; Cheung, Y. W.; Chum, S. *Macromolecules* **1999**, *32*, 6221−6235.
(4) Goderis, B.; Peeters, M.; Mathot, V. B. F.; Koch, M. H. J.; Bras, W.; Ryan, A. J.; Reynaers, H. *J. Polym. Sci., Part B: Polym. Phys.* **2000**, *38*, 1975−1991.
(5) Goderis, B.; Reynaers, H.; Koch, M. H. J. *Macromolecules* **2002**, *35*, 5840−5853.
(6) Alamo, R.; Domszy, R.; Mandelkern, L. *J. Phys. Chem.* **1984**, *88*, 6587−6595.
(7) Schouterden, P.; Riekel, C.; Koch, M.; Groeninckx, G.; Reynaers, H. *Polym. Bull. (Berlin)* **1985**, *13*, 533−539.
(8) Schouterden, P.; Groeninckx, G.; Vanderheijden, B.; Jansen, F. *Polymer* **1987**, *28*, 2099−2104.
(9) Schouterden, P.; Vandermarliere, M.; Riekel, C.; Koch, M. H. J.; Groeninckx, G.; Reynaers, H. *Macromolecules* **1989**, *22*, 237−244.
(10) Mirabella, F. M.; Ford, E. A. *J. Polym. Sci., Part B: Polym. Phys.* **1987**, *25*, 777−790.
(11) Perez, E.; Vanderhart, D. L.; Crist, B.; Howard, P. R. *Macromolecules* **1987**, *20*, 78−87.
(12) Mirabella, F. M.; Westphal, S. P.; Fernando, P. L.; Ford, E. A.; Williams, J. G. *J. Polym. Sci., Part B: Polym. Phys.* **1988**, *26*, 1995−2005.
(13) Mathot, V. B. F.; Pijpers, M. F. J. *J. Appl. Polym. Sci.* **1990**, *39*, 979−994.
(14) Defoor, F.; Groeninckx, G.; Schouterden, P.; Vanderheijden, B. *Polymer* **1992**, *33*, 3878−3883.
(15) Defoor, F.; Groeninckx, G.; Reynaers, H.; Schouterden, P.; Vanderheijden, B. *Macromolecules* **1993**, *26*, 2575−2582.
(16) Defoor, F.; Groeninckx, G.; Reynaers, H.; Schouterden, P.; Vanderheijden, B. *J. Appl. Polym. Sci.* **1993**, *47*, 1839−1848.
(17) Mirabella, F. M. *J. Polym. Sci., Part B: Polym. Phys.* **2001**, *39*, 2800−2818.
(18) Crist, B.; Claudio, E. S. *Macromolecules* **1999**, *32*, 8945−8951.
(19) Crist, B.; Howard, P. R. *Macromolecules* **1999**, *32*, 3057−3067.
(20) Crist, B.; Williams, D. N. *J. Macromol. Sci.—Phys.* **2000**, *B39*, 1−13.
(21) Androsch, R. *Polymer* **1999**, *40*, 2805−2812.
(22) Androsch, R.; Wunderlich, B. *Macromolecules* **1999**, *32*, 7238−7247.
(23) Mathot, V. B. F.; Scherrenberg, R. L.; Pijpers, M. F. J.; Bras, W. *J. Therm. Anal.* **1996**, *46*, 681−718.
(24) Mathot, V. B. F.; Scherrenberg, R. L.; Pijpers, T. F. J. *Polymer* **1998**, *39*, 4541−4559.
(25) Bensason, S.; Minick, J.; Moet, A.; Chum, S.; Hiltner, A.; Baer, E. *J. Polym. Sci., Part B: Polym. Phys.* **1996**, *34*, 1301−1315.
(26) Go, S.; Mandelke, L.; Prudhomm, R.; Stein, R. *J. Polym. Sci., Part B: Polym. Phys.* **1974**, *12*, 1485−1490.
(27) Mandelkern, L.; Maxfield, J. *J. Polym. Sci., Part B: Polym. Phys.* **1979**, *17*, 1913−1927.
(28) Koberstein, J.; Russell, T. P.; Stein, R. S. *J. Polym. Sci., Part B: Polym. Phys.* **1979**, *17*, 1719−1730.
(29) Stein, R. S.; Cronauer, J.; Zachmann, H. G. *J. Mol. Struct.* **1996**, *383*, 19−22.
(30) Akpalu, Y. A.; Kielhorn, L.; Hsiao, B. S.; Stein, R. S.; Russell, T. P.; van Egmond, J.; Muthukumar, M. *Macromolecules* **1999**, *32*, 765−770.
(31) Wang, Z.-G.; Hsiao, B. S.; Sirota, E. B.; Agarwal, P.; Srinivas, S. *Macromolecules* **2000**, *33*, 978−989.
(32) Jokela, K.; Vaananen, A.; Torkkeli, M.; Starck, P.; Serimaa, R.; Lofgren, B.; Seppala, J. *J. Polym. Sci., Part B: Polym. Phys.* **2001**, *39*, 1860−1875.
(33) Beaucage, G.; Sukumaran, S.; Rane, S.; Kohls, D. J. *J. Polym. Sci. Pt. B—Polym. Phys.* **1998**, *36*, 3147−3154.
(34) Akpalu, Y. A. Doctoral Thesis, Polymer Science and Engineering; University of Massachusetts: Amherst, 1998.
(35) Somwangthanaroj, A.; Lee, E. C.; Solomon, M. J. *Macromolecules* **2003**, *36*, 2333−2342.
(36) Pogodina, N. V.; Siddiquee, S. K.; van Egmond, J. W.; Winter, H. H. *Macromolecules* **1999**, *32*, 1167−1174.
(37) Kyu, T.; Hu, S.-R.; Stein, R. S. *J. Polym. Sci., Part B: Polym. Phys.* **1987**, *25*, 89−103.
(38) Akpalu, Y. A.; Lin, Y. Y. *J. Polym. Sci., Part B: Polym. Phys.* **2002**, *40*, 2714−2727.
(39) Peeters, M.; Goderis, B.; Vonk, C.; Reynaers, H.; Mathot, V. *J. Polym. Sci.: Part B: Polym. Phys.* **1997**, *35*, 2689−2713.
(40) Vanden Eynde, S.; Mathot, V. B. F.; Koch, M. H. J.; Reynaers, H. *Polymer* **2000**, *41*, 4889−4900.
(41) Litvinov, V. M.; Mathot, V. B. F. *Solid State Nucl. Magn. Reson.* **2002**, *22*, 218−234.
(42) Alizadeh, A.; Xu, J. N.; Subramaniam, C.; Richardson, L.; Marand, H. *Abstr. Pap. Am. Chem. Soc.* **1999**, *218*, 136−PMSE.
(43) Mandelkern, L.; Glotin, M.; Benson, R. A. *Macromolecules* **1981**, *14*, 22−34.
(44) Failla, M. D.; Lucas, J. C.; Mandelkern, L. *Macromolecules* **1994**, *27*, 1334−1337.

(45) Yoon, D. Y.; Stein, R. S. *J. Polym. Sci., Part B: Polym. Phys.* **1974**, *12*, 735−761.
(46) Stein, R. S.; Keane, J. J. *J. Polym. Sci.* **1955**, *17*, 21−44.
(47) Akpalu, Y. A.; Amis, E. J. *J. Chem. Phys.* **2000**, *113*, 392−403.
(48) Murthy, N. S.; Akkapeddi, M. K.; Orts, W. J. *Macromolecules* **1998**, *31*, 142−152.
(49) Crist, B. *J. Macromol. Sci.—Phys.* **2000**, *B39*, 493−518.
(50) Crist, B. *J. Polym. Sci., Part B: Polym. Phys.* **2001**, *39*, 2454−2460.
(51) Strobl, G. R.; Schneider, M. *J. Polym. Sci., Part B: Polym. Phys.* **1980**, *18*, 1343−1359.
(52) Vonk, C. G.; Pijpers, A. P. *J. Polym. Sci., Part B: Polym. Phys.* **1985**, *23*, 2517−2537.
(53) Stein, R. S.; Rhodes, M. B. *J. Appl. Phys.* **1960**, *31*, 1873−1884.
(54) Clough, S.; Vanaarts, J.; Stein, R. S. *J. Appl. Phys.* **1965**, *36*, 3072−3085.
(55) Stein, R. S.; Chu, W. *J. Polym. Sci., Part A-2: Polym. Phys.* **1970**, *8*, 1137−1157.
(56) Samuels, R. J. *J. Polym. Sci., Part B: Polym. Phys.* **1971**, *9*, 2165−2246.
(57) Samuels, R. J. *J. Polym. Sci., Part B: Polym. Phys.* **1974**, *12*, 1417−1439.
(58) Stein, R. S.; Picot, C. *J. Polym. Sci., Part A-2: Polym. Phys.* **1970**, *8*, 1955−1969.
(59) Tabar, R. J.; Leite-James, P.; Stein, R. S. *J. Polym. Sci., Part B−Polym. Phys.* **1985**, *23*, 2085−2107.
(60) Goderis, B.; Reynaers, H.; Koch, M. H. J.; Mathot, V. B. F. *J. Polym. Sci., Part B: Polym. Phys.* **1999**, *37*, 1715−1738.
(61) Flory, P. J. *Trans. Faraday Soc.* **1955**, *51*, 848−857.
(62) Sanchez, I. C.; Eby, R. K. *Macromolecules* **1975**, *8*, 638−641.
(63) Kim, M. H.; Phillips, P. J.; Lin, J. S. *J. Polym. Sci., Part B: Polym. Phys.* **2000**, *38*, 154−170.
(64) Marand, H.; Xu, J. N.; Srinivas, S. *Macromolecules* **1998**, *31*, 8219−8229.
(65) Hoffman, J. D.; Weeks, J. J. *J. Res. Natl. Bur. Stand., A: Phys. Chem.* **1962**, *66*, 13−28.
(66) Flory, P. J.; Vrij, A. *J. Am. Chem. Soc.* **1963**, *85*, 3548−3553.
(67) Hoffman, J. D.; Davis, G. T.; Lauritzen, J. I. In *Treatise on Solid State Chemistry*; Hanny, N. B., Ed.; Plenum Press: New York, 1976; Vol. 3.
(68) Defoor, F.; Groeninckx, G.; Schouterden, P.; Vanderheijden, B. *Polymer* **1992**, *33*, 5186−5190.
(69) Akpalu, Y. A.; Amis, E. J. *J. Chem. Phys.* **1999**, *111*, 8686−8695.
(70) Guinier, A.; Fournet, G. *Small-Angle Scattering of X-rays*; Wiley: London, 1955.
(71) Minick, J.; Moet, A.; Hiltner, A.; Baer, E.; Chum, S. P. *J. Appl. Polym. Sci.* **1995**, *58*, 1371−1384.
(72) Alamo, R. G.; Mandelkern, L. *Macromolecules* **1991**, *24*, 6480−6493.
(73) Puig, C. C.; Aviles, M. V.; Joskowicz, P.; Diaz, A. *J. Appl. Polym. Sci.* **2001**, *79*, 2022−2028.
(74) Cruz, C. S.; Stribeck, N.; Zachmann, H. G.; Calleja, F. J. B. *Macromolecules* **1991**, *24*, 5980−5990.
(75) Clough, S.; Rhodes, M. B.; Stein, R. S. *J. Polym. Sci., Part C: Polym. Symp.* **1967**, 1−12.
(76) Schultz, J. M.; Lin, J. S.; Hendricks, R. W. *J. Appl. Crystallogr.* **1978**, *11*, 551−557.
(77) Vonk, C. G.; Koga, Y. *J. Polym. Sci., Part B: Polym. Phys.* **1985**, *23*, 2539−2548.

MA049435N